Nanoscale

Accepted Manuscript

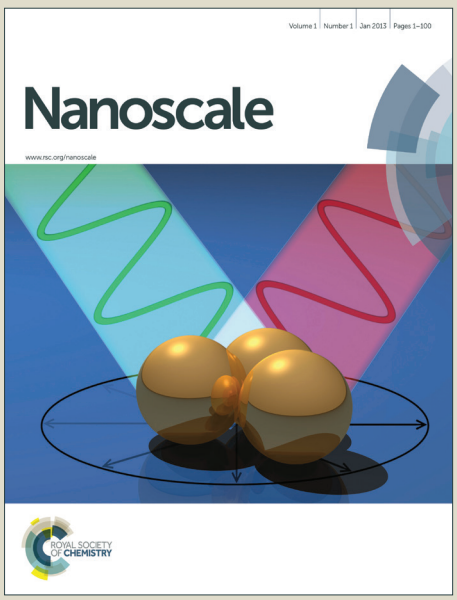

ROYAL SOCIETY OF CHEMISTRY

www.rsc.org/nanoscale

Nanoscale

RSCPublishing

COMMUNICATION

Hierarchical 3D TiO_2@Fe_2O_3 nanoframework arrays as high-performance anode materials

Cite this: DOI: 10.1039/xoxxoooooox

Lin Gao, Hao Hu, Guojian Li, Qiancheng Zhu and Ying Yu*

Received ooth January 2012,
Accepted ooth January 2012

DOI: 10.1039/xoxxoooooox

www.rsc.org/

Hierarchical 3D TiO_2@Fe_2O_3 nanoframework arrays grown on Ti substrate are synthesized via a facile hydrothermal reaction. As the synergetic effect of this hybrid material, the TiO_2@Fe_2O_3 electrode shows superior rate capability and cycling performance to bare TiO_2 and Fe_2O_3 electrodes.

TiO_2 with various morphologies such as nanotubes,[1] nanowires,[2] nanosheets,[4] mesoporous microspheres[5] and so on have been extensively studied as the candidate for the next-generation anode materials. Amongst them, nanosheet TiO_2 with the two-dimensional morphology similar to graphene[6] shows efficient rate and cycling performance for rechargeable lithium-ion batteries (LIBs).[7-9] However, it is well known that the TiO_2 possesses relatively low theoretical capacity of 335 mAh g^{-1} even with the maximum accommodation of one Li^+ per TiO_2 unit ($Li_{1.0}TiO_2$),[10] which seriously hinders its potential large-scale applications in commercialization. To circumvent above issues, a number of metallic oxides (MO) with high specific capacity (700-1000 mAh g^{-1}) were therefore used to synthesize hybrid TiO_2-MO nanocomposites. By this way, the advantages of the high capability for MO and the electrochemical stability of TiO_2 will be incorporated together. For example, it has been reported by Zeng's group that highly uniform TiO_2/SnO_2/carbon hybrid nanofibers showed enhanced lithium storage performance.[11] On the other hand, Fe_2O_3 nanorods were also grafted within TiO_2 nanotubes and have impressed cycling performance by Lou's group.[12] Most recently, Co_3O_4, Fe_2O_3, Fe_3O_4 and CuO grown on TiO_2 fibres with hierarchical heterostructures have also been fabricated by Wang's group and displayed improved electrochemical performance.[13] Among above mentioned materials, α-Fe_2O_3 with higher theoretical capacity (1007 mAh g^{-1}) than commercial graphite-based (372 mAh g^{-1}) anode materials,[14,15] low cost and environmental friendliness, inevitably has received considerable interests.[16-17] Nevertheless, to the best of our knowledge, there has been no report about Fe_2O_3 nanorods anchored on two dimensional (2D) TiO_2 nanosheets so far, in which TiO_2 nanosheets have been considered as the state-of-the-art materials for LIBs.[7-9]

Herein, for the first time, we developed a facile hydrothermal method instead of conventional template and electrodeposition strategies to successfully fabricate hierarchical three-dimensional (3D) TiO_2@Fe_2O_3 core-shell nanoframework arrays. To overcome the problems of the large volume expansion and grain aggregation for Fe_2O_3,[18] mesoporous TiO_2 nanosheets directly grown on Ti substrate were followed by the uniform deposition of Fe_2O_3 nanorods, in which the nanorod structure of Fe_2O_3 not only provides direct and open channels for Li ions, but also it can accommodate the volume expansion in virtue of the space between and within the mesoporous nanorod structure.[16] Besides, the 3D TiO_2@Fe_2O_3 nanoframework arrays possessing synergetic effect as the electrode without any conductive agent and binder demonstrate potential applications.[19,20] The synergetic effect mentioned above can be summarized as follows. Firstly, the aggregation and volume expansion of Fe_2O_3 can be effectively avoided with the mesoporous TiO_2 nanosheets as the scaffold in the process of lithium/delithium reaction.[21] Simultaneously, the free space between nanorod and mesoporous structures can provide open channels and more contact area for the transportation of lithium ions and electrons, allowing superior lithium storage performance. Secondly, the deposition of Fe_2O_3 nanorods on TiO_2 nanosheets not only showed enhanced capacity, but also well integrated the electrochemical advantages of these two functional materials in the form of hierarchical structure.

Scheme. 1 shows the evolution process of hierarchical TiO_2@Fe_2O_3 nanoframework arrays. In the first step, TiO_2 nanosheet arrays were prepared via the routine hydrothermal reaction reported previously.[22] Subsequently, 3D TiO_2@FeOOH nanoframework arrays were synthesized with the hydrolysis of $FeCl_3$ and the final hierarchical TiO_2@Fe_2O_3 arrays were in-situ formed after the calcination at 500℃ for 1h. The detailed experimental process for the preparation is shown in supporting information (ESI†).

Surprisingly, it is found that the morphology of TiO_2 arrays can be controlled by varying the amount of NaCl (Fig. S1, ESI†) in the process of hydrothermal reaction. Scanning electron microscopy (SEM) measurement was introduced to observe the morphology of TiO_2 arrays in different conditions. It can be seen that the TiO_2 nanosheets were formed when the concentration of NaCl was 0 and 1 M, and the morphology of the above two samples almost had no difference according to the SEM images shown in Figs. S1a† and S1b†. However, both TiO_2 nanowires and nanosheets were prepared in the meantime (seen in Fig. S1c†) when the concentration of NaCl increased to 2 M. There was only TiO_2 nanowire clearly observed in

Fig. S1d† if the concentration of NaCl was 3 M. Therefore, the content of NaCl had great effect on the morphology of TiO_2 arrays which controlled the nucleation and growth processes.[23]

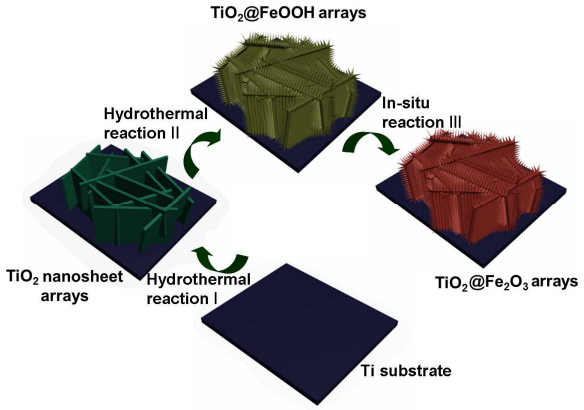

Scheme. 1. Schematic illustration for the fabrication of 3D $TiO_2@Fe_2O_3$ nanoframework arrays.

It is fortunately found that the morphology of $TiO_2@Fe_2O_3$ arrays were also varied with different amounts of $FeCl_3·6H_2O$ and Na_2SO_4 as shown in Fig. S2†. When the addition of $FeCl_3·6H_2O$ was 9.3 mM and 18.6 mM, α-Fe_2O_3 nanorods with the length of around 100 nm and 200 nm were uniformly deposited on TiO_2 nanosheets respectively, which can be clearly seen in Figs. S2a~S2d†. If the amount of $FeCl_3·6H_2O$ increased to 25 mM, however, there was no nanosheet observed in Fig. S2e†, which may be due to the excess of $FeCl_3·6H_2O$. All of the TiO_2 nanosheets were covered by Fe_2O_3 nanorods and were agglomerated to bunches after calcinaiton (Fig. S2f†). Transmission electron microscopy (TEM) analysis was also introduced to further investigate the morphology of bare TiO_2 nanosheet arrays and 3D $TiO_2@Fe_2O_3$ arrays. Fig. 1a showed the SEM image of TiO_2 nanosheets with size of around 1 μm and thickness of 50 nm. However, $TiO_2@Fe_2O_3$ nanoframework showed worm-like morphology with size of ~500 nm after uniformly deposited Fe_2O_3 nanorods (Fig. 1b). The inset is the close observation of the single $TiO_2@Fe_2O_3$ framework, in which Fe_2O_3 nanorods with length of ~200 nm were delicately anchored on the TiO_2 nanosheet backbone, leading to the obvious swelling of $TiO_2@Fe_2O_3$ nanoframeworks compared to bare TiO_2 nanosheet arrays. The calculated mass ratio of TiO_2 (57.1%) and Fe_2O_3 (42.9%) was obtained by weighing the active materials of TiO_2 and $TiO_2@Fe_2O_3$ respectively through subtracting the mass of substrates. The balance (Sartorius, BT 125D) was used to weight the mass. From the enlarged TEM image of the single TiO_2 nanosheet in Fig. 1c, we can conclude that the TiO_2 nanosheets were composed of nanoparticles of diameter around 20 nm and possessed mesoporous nanostructure. The pore size distribution of TiO_2 nanosheets is shown in Fig. S3a† and the inset is the TEM image of the individual TiO_2 nanosheet. The remarkable lattice fringes with 0.35 nm interplanar spacing of anatase TiO_2 were observed via a high resolution TEM (HRTEM) image (Fig. 1d), which corresponded to the typical (101) plane. Mesoporous Fe_2O_3 nanorods with size of around 200 nm were observed distinctly in the enlarged TEM image of $TiO_2@Fe_2O_3$ (Fig. 1e) and the inset was the full view of the single 3D $TiO_2@Fe_2O_3$ composite. These images agreed well with the SEM results. N_2 adsorption-desorption curve was introduced to further clarify the nanostructure of $TiO_2@Fe_2O_3$ (Fig. S3b†). Type IV curve with H2 hysteresis loop and the pore size distribution concentrated at 2~11 nm revealed the mesoporous nanostructure of the material. Typical lattice fringes of α-Fe_2O_3 with interplanar distance 0.27 nm were shown in the HRTEM image (Fig. 1f), further demonstrating that Fe_2O_3 nanorods were indeed tightly deposited on TiO_2 nanosheets.

The mechanistic comparison of lithium ion diffusion between bare TiO_2 nanosheet arrays and the $TiO_2@Fe_2O_3$ nanframework arrays is depicted in Fig. 2a. It can be clearly seen that there were more direct channels for lithium ion diffusion because of the existence of Fe_2O_3 nanorods compared with bare 2D TiO_2, which thereafter provided more contact area between electrolyte and active materials for potential high-performance LIBs.[24] It further illustrates the presence of synergetic effect in the $TiO_2@Fe_2O_3$ arrays. The nyquist plots (The inset is the magnified nyquist plots and the equivalent circuit model) of $TiO_2@Fe_2O_3$, TiO_2 and Fe_2O_3 electrodes are presented in Fig S4a†. Simultaneously, the lithium ion diffusion coefficients of $TiO_2@Fe_2O_3$ ($D_{Li}=8.5\times10^{-11}$ cm^2 s^{-1}), TiO_2 ($D_{Li}=2.6\times10^{-11}$ cm^2 s^{-1}), Fe_2O_3 ($D_{Li}=1.9\times10^{-11}$ cm^2 s^{-1}) were calculated according to the relation between low frequency and real resistance in Fig S4b†. The

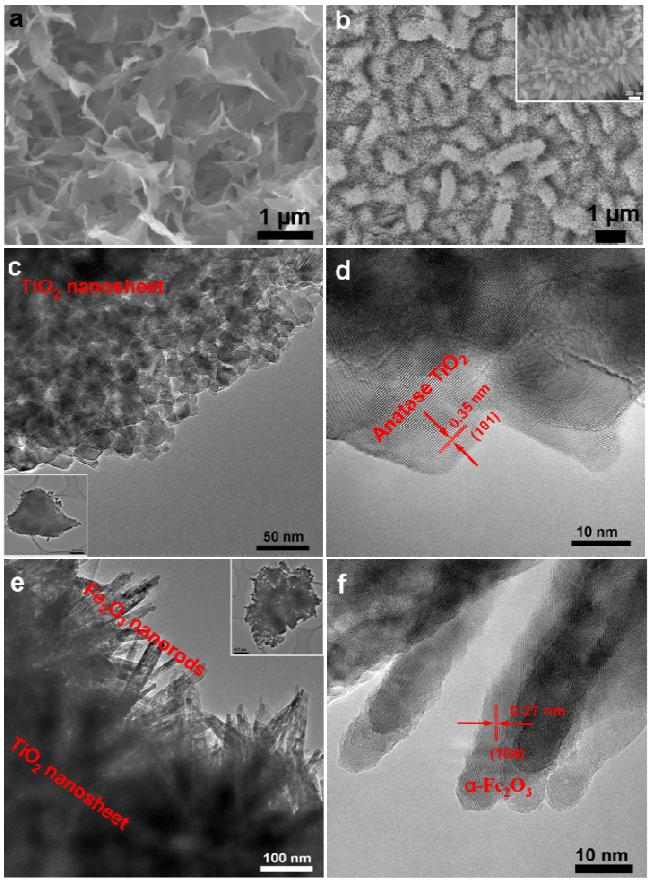

Fig. 1. SEM images of (a) TiO_2 nanosheet arrays and (b) $TiO_2@Fe_2O_3$ arrays (The inset is the magnified image of single worm-like structure); (c) TEM images (The inset is the magnified image of the edge) and (d) HRTEM images of TiO_2 nanosheet arrays; (e) TEM images of $TiO_2@Fe_2O_3$ arrays (The inset is the magnified image of the edge) and (f) HRTEM image of the anchored α-Fe_2O_3 nanorods

data indicated the improved lithium ion diffusion after the anchor of Fe_2O_3 nanorods and verified the mechanism illustrated in Fig. 2a.[25]

X-ray diffraction (XRD) patterns of the prepared Fe_2O_3 nanorods, TiO_2 nanosheets, $TiO_2@FeOOH$ (the intermediate of $TiO_2@Fe_2O_3$) and $TiO_2@Fe_2O_3$ nanoframeworks are displayed in Fig. 2b. There

was only typical diffraction peaks of α-Fe_2O_3 (hemetite, JCPDS card no. 330664) for Fe_2O_3 nanorods, while there were diffraction peaks ascribed to TiO_2-B for TiO_2 nanosheets, TiO_2@FeOOH and TiO_2@Fe_2O_3 nanoframeworks, which was in accordance with previous report.[22] Typical reflection peaks of FeOOH (JCPDS card No.22-0353) for TiO_2@FeOOH combined with the peaks of α-Fe_2O_3 for TiO_2@Fe_2O_3 were also detected besides the peaks of anatase TiO_2 (JCPDS card No.21-1272) and TiO_2-B, revealing the existence of well crystallized Fe_2O_3 nanorods and TiO_2 nanosheets for the final TiO_2@Fe_2O_3. All of the diffraction peaks of TiO_2 nanosheet were well classified to typical anatase TiO_2 without any purity. The comparison of XRD patterns for TiO_2@Fe_2O_3 prepared with different amounts of $FeCl_3 \cdot 6H_2O$ and Na_2SO_4 is shown in Fig. S5†. It is obviously seen that with the increased amount of $FeCl_3 \cdot 6H_2O$, the intensity of the reflection peaks for α-Fe_2O_3 became stronger, demonstrating the increased content of Fe_2O_3 in the sample of TiO_2@Fe_2O_3.

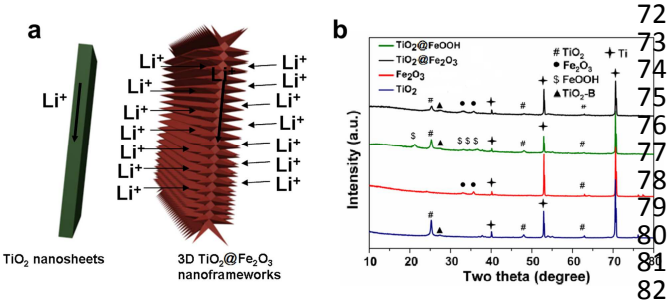

Fig. 2. (a) Schematic comparison of Li ion diffusion between TiO_2 nanosheet arrays and TiO_2@Fe_2O_3 arrays. (b) XRD patterns of TiO_2 nanosheet arrays, pure Fe_2O_3 nanorods, TiO_2@FeOOH and final TiO_2@Fe_2O_3 arrays.

In order to thoroughly elucidate the improved electrochemical performance for the TiO_2@Fe_2O_3 electrode, Fe_2O_3 nanorod (SEM image shown in Fig. S6†) and TiO_2 nanosheet arrays were also prepared to assemble circular electrodes. The optical images of the prepared samples and bare Ti substrate (Chinese coin for scale bar) are presented in Fig. S7†. Cyclic voltametry (CV) curves of the TiO_2@Fe_2O_3 electrode in the initial three charge-discharge cycles are displayed in Fig. 3 with the scanning rate of 0.5 mV s^{-1} in the window voltage of 0.05~3 V. Typical two cathodic peaks at 1.5 and 0.6 V were shown in the first cycle, corresponding to the process of reduction for Fe_2O_3 from Fe^{3+} to $Fe^{2+}$and Fe^0 combined with the formation of SEI film. [16,28-29] There were two oxidation peaks at 1.7 and 2.4 V corresponding to the extraction of Li ions from Fe_2O_3 and TiO_2 for TiO_2@Fe_2O_3 electrode. In the second cycle, there was a slight increase of oxidation peaks at 0.65, 0.8, and 1.7 V with the lower intensity, indicating the existence of irreversible reaction ascribed to formation of SEI film. [28,29] The oxidation and reduction peaks almost had no change in the subsequent cycle, demonstrating the good reversibility of the TiO_2@Fe_2O_3 electrode.

The galvanostatic charge-discharge curves of TiO_2@Fe_2O_3 electrode in the 1st, 65th and 103rd cycles with the voltage window of 0.05 V~3 V at 200 mA g^{-1} are shown in Fig. 3b. The plateau voltages in the first cycle were in good agreement with the oxidation and reduction peaks in the above mentioned CVs. The charge-discharge curves of TiO_2@Fe_2O_3, bare TiO_2 and bare Fe_2O_3 electrodes at different current densities are presented in Fig. S8† to illustrate the different electrochemical reactions in terms of the lithium/delithium process. The cycling performance of bare TiO_2 and Fe_2O_3 electrodes were also introduced to further illustrate the superior cycling performance of the TiO_2@Fe_2O_3 electrode in Fig. 3c. TiO_2 nanosheet electrode showed stable cyclability with almost no capacity loss after 100 cycles but with only one-forth initial capacity. For Fe_2O_3 electrode, its specific capacity degraded severely through 100 cycles at 200 mA g^{-1} since only 112.9 mAh g^{-1} remained. In contrast, the TiO_2@Fe_2O_3 electrode had the most excellent cyclability actually with the increasing specific capacity starting from the 67th cycle and still possessed capacity of 430.2 mAh g^{-1} after 103 cycles. This phenomenon is not uncommon for Fe_2O_3 and other metal oxide materials. [26-31] It is generally attributed to the formation of polymeric/gel-like film around the active materials caused by the decomposition of the electrolyte at low potential, which enabled the mechanical cohesion and delivered excess capacity through a so called "pseudo-capacity-type" behavior. On the other hand, the synergetic effect of the hybrid materials was also the main reason for the increased capacity as for bare Fe_2O_3 nanorod arrays, there was no capacity increase observed. The corresponding coulombic efficiency of TiO_2@Fe_2O_3 electrode was almost 100% in the over process. The rate performance of above mentioned three electrodes are presented in Fig. 3d, in which the TiO_2@Fe_2O_3 electrode showed much higher capacity than bare TiO_2 and Fe_2O_3 electrodes. Nevertheless, the specific capacity for TiO_2@Fe_2O_3 electrode decayed severely in case of different current densities, which might be attributed to the partially irreversible formation of Fe nanoparticles in the initial electrochemical reaction:

$$Fe_2O_3+6Li^++6e^- \leftrightarrow 2Fe+3Li_2O. \quad (1)$$

The TiO_2@Fe_2O_3 electrode still showed the most competitive rate capability with capacity of 168.3 mAh g^{-1} at 1600 mA g^{-1}, much higher than the capacity of bare TiO_2 and Fe_2O_3 electrodes. The coulombic efficiency of the above three electrodes at the condition of cycling and rate performance test is presented in Fig. S9†. The TiO_2@Fe_2O_3 electrode possessed a little bit better coulombic efficiency than that of TiO_2 and Fe_2O_3 electrodes although all of the electrodes had good efficiency, which is significantly important to the applications of the materials.

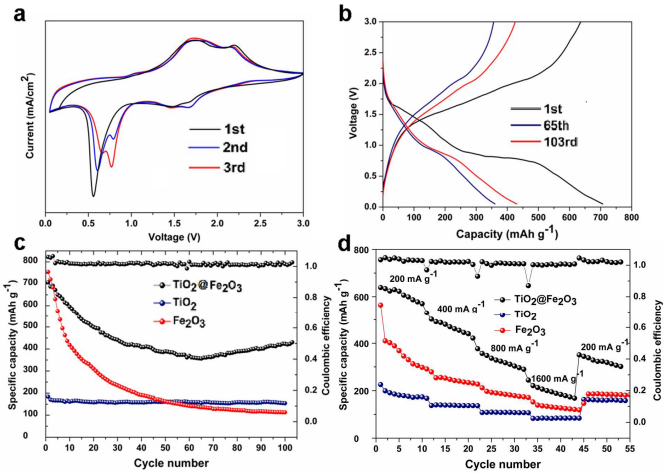

Fig. 3. Electrode performance: (a) CV curves of TiO_2@Fe_2O_3 electrode; (b) the 1st, 65th and 103rd galvanostatic charge-discharge profiles of TiO_2@Fe_2O_3 electrode; (c) cycling performance and coulombic efficiency of TiO_2@Fe_2O_3, TiO_2 and Fe_2O_3 electrodes at 200 mA g^{-1}; (d) rate performance and coulombic efficiency of TiO_2@Fe_2O_3, TiO_2 and Fe_2O_3 electrodes at different current densities.

In summary, we have successfully synthesized hierarchical TiO_2@Fe_2O_3 nanoframework arrays. As a result of the buffering effect of mesoporous TiO_2 nanosheets and the abundant free space between Fe_2O_3 nanorods and mesoprous structures, the hybrid

TiO_2@Fe_2O_3 electrode shows superior cycling performance and rate capability to bare TiO_2 and Fe_2O_3 electrodes. The synergetic effect of the hybrid materials also has great effect on the electrochemical properties. Substantially, the introduction of Fe_2O_3 nanorodes plays a significant role in advancing the specific capacity of the TiO_2@Fe_2O_3 electrode and the mesoporous TiO_2 nanosheets as the scaffold has the advantage for keeping the excellent cyclability. It is expected that the special fabrication strategies mentioned in this article will be widely utilized to construct other hybrid nanostructures for improving the electrochemical performance of low-capacity materials such as $Li_4Ti_5O_{12}$ and graphite.

Acknowledgements

This work was financially supported by the National Natural Science Foundation of China (No. 21377044), Wuhan Planning Project of Science and Technology (No. 2014010101010023), the Key Project of Natural Science Foundation of Hubei Province (No.2011CDA092) and self-determined research funds of CCNU from the colleges' basic research and operation of MOE (No. CCNU13F027).

Institute of Nanoscience and Nanotechnology, College of Physical Science and Technology, Central China Normal University, China

* Corresponding author. Tel: 86-27-67867037. Fax: 86-27-67861175. Email: yuying01@mail.ccnu.edu.cn

†Electronic Supplementary Information (ESI) available: Detailed experimental methods and supplementary figures are shown in supplementary imformation. See DOI: 10.1039/c000000x/

Notes and references

1 Q. L. Wu, J. Li, R. D. Deshpande, N. Subramanian, S. E. Rankin, F. Yang and Y. T. Cheng, *J. Phys. Chem. C*, 2012, 116, 18669.
2 G. Armstrong, A. R. Armstrong, P. G. Bruce, P. Reale and B. Scrosati, *Adv. Mater*, 2006, 18, 2597.
3 Y. P. Tang, X. X. Tan, G. Y. Hou, H. Z. Cao and G. Q. Zheng, *Electrochim. Acta,* 2012, 78, 154.
4 J. S. Chen and X. W. Lou, *Electrochem. Commun*, 2009, 11, 2332.
5 J. Wang, Y. K. Zhou, Y. Y. Hu, R. O'Hayre and Z. P. Shao, *J. Phys. Chem. C*, 2011, 115, 2529.
6 Z. L. Wang, Dan Xu, J.J. Xu, L. L. Zhang and X. B. Zhang, *Adv. Funct. Mater*, 2012, 22, 3699.
7 J. S. Chen, Y. L. Tan, C. M. Li, Y. L. Cheah, D. Luan, S. Madhavi, F. Y. C. Boey, L. A. Archer and X. W. Lou, *J. Am Chem. Soc*, 2010, 132, 6124.
8 S. H. Liu, H. P. Jia, L. Han, J. L. Wang, P, F. Gao, D. D. Xu, J. Yang and S. Che, *Adv. Mater*. 2012, 24, 3201.
9 J. S. Chen and X. W. Lou, materialstoday, 2012, 15, 246.
10 Z. G. Yang, D. Choi, S. Kerisit, K. M. Rosso, D. H. Wang, J. Zhang, G. Graff and Jun Liu, *J. Power Source*, 2009, 192, 588.
11 Z. X. Yang, Q. Meng, Z. P. Guo, X. B. Yu, T. L. Guo and R. Zeng, *J. Mater. Chem. A*, 2013, 1, 10395.
12 L. Yu, Z. Y. Wang, L. Zhang, H. B. Wu and X. W. Lou, *J. Mater. Chem. A*, 2013, 1, 122.
13 H. G. Wang, D. L. Ma, X. L. Huang, Y. Huang and X. B Zhang, *Sci. Rep.* 2012, 2, 1.
14 D. Lei, M. Zhang, B. H. Qu, L. B. Chen, Y. G. Wang, E. Zhang, Z. Xu, Q.H. Li and T. H. Wang, *Nanoscale*, 2012, 4, 3422.
15 M. Endo , C. Kim, K. Nishimura, T. Fujino and K. Miyashita, Carbon, 2000, 38, 183.
16 Y. Q. Song, S.S. Qin, Y. W. Zhang, W. Q. Gao and J. P. Liu, *J. Phys. Chem. C*, 2010, 114, 21158.
17 J. Chen, L. Xu, W. Y. Li and X. L. Gou, *Adv. Mater*. 2005, 17, 582.
18 X. J. Zhu, Y. W. Zhu, S. Murali, M. D. Stoller and R. S. Ruoff, *ACS Nano*, 2011, 5, 3333.
19 D. L. Ma, Z. Y. Cao, H. G. Wang, X. L. Huang, L. M.Wang and X. B Zhang, *Energy Environ. Sci*, 2012, 5, 8538.
20 Z. L. Wang, D. Xu, H. G Wang, Z. Wu and X. B. Zhang, *ACS Nano*,2013, 7, 2422.
21 Y. Huang, X. L. Huang, J. S. Lian, D. Xu, L. M. Wang and X. B. Zhang, *J. Mater. Chem.* 2012, 22, 2844.
22 C. C. Wang, X. T. Zhang, Y. L. Zhang, Y. Jia, J. K. Yang, P. P. Sun and Y. C. Liu. *J. Phys. Chem. C*, 2011, 115, 22276.
23 Z. L. He, Z. F. Zhu, J. Q. Li, J. Q. Zhou and N. Wei. *J. Hazard. Mater,* 2011, 190, 133.
24 W. W. Zhou, C.W. Cheng, J. P. Liu, Y. Y. Tay, J. Jiang, X. T. Jia, J. X. Zhang, H. Gong, H. H. Hng, T. Yu and J. H. Fan. *Adv. Funct. Mater*, 2011, 21, 2439.
25 W. Wang, Y. Y. Guo, L. X. Liu, S. X. Wang, X. J. Yang and H. Guo, *J. Power Source,* 2014, 245, 624.
26 T. Zhu, J.S. Chen and X. W. Lou, *J. Phys. Chem. C*, 2011, 115, 9814.
27 Z. Y. Wang, D. Y. Luan, S. Madhavi, Y. Hu and X. W. Lou, *Energy Environ. Sci,* 2012, 5, 5252.
28 J. S. Luo, X. H. Xia, Y. S. Luo, Cao Guan, J. L. Liu, X. Y. Qi, C. F. Ng , T. Yu, H. Zhang and H. J. Fan, *Adv. Energy Mater*, 2013, 3, 737.
29 Y. S. Luo, J. S. Luo, J. Jiang, W. W. Zhou, H. P. Yang, X. Y. Qi, H. Zhang, H. J. Fan, D.Y. W. Yu, C. M. Li and T. Yu, *Energy Environ. Sci*, 2012, 5, 6559.
30 Q. Q. Xiong, J. P. Tu, X. H. Xia, X. Y. Zhao, C. D. Gu and X. L. Wang, *Nanoscale,* 2013, 5, 7906.
31 M. Kundu, C. C. A. Ng, D. Y. Petrovykh and L. F. Liu, *Chem. Commun*, 2013, 49, 8459.

